Korean J. Chem. Eng., 36(7), 1148-1156 (2019)
DOI: 10.1007/s11814-019-0297-8

pISSN: 0256-1115
eISSN: 1975-7220

Green synthesis of TiO_2 nanoparticles using *Cajanus cajan* extract and their use in controlling the fouling of ultrafiltration PVDF membranes

Zeenat Arif*,†, Naresh Kumar Sethy*, Lata Kumari, Pradeep Kumar Mishra*, and Bhawna Verma***

*Department of Chemical Engineering and Technology, Indian Institute of Technology (BHU), Varanasi, India
**Department of Chemistry, Indian Institute of Technology (BHU), Varanasi, India
(*Received 13 March 2019 • accepted 12 May 2019*)

Abstract−Polyvinylidene fluoride (PVDF)/TiO_2 composite ultrafiltration membranes were fabricated using different loadings of TiO_2 NPs synthesized by the green route using an extract of *Cajanus cajan*. XRD analysis confirmed the synthesis of TiO_2 nanoparticles of size 10 nm using Debye Scherrer's equation. High hydrophobicity of PVDF restricts its successful application due to fouling in the membrane. Therefore, composite membranes were prepared via the phase inversion route and characterized by contact angle and permeation tests. The BSA filtration experiments revealed that membrane with 0.5 wt% of TiO_2 exhibits excellent hydrophilicity, permeation flux, high rejection ratio, and good antifouling performance. It was observed that the fouling characteristic of the membrane is governed by the surface roughness of the membrane, and with increasing loading of TiO_2 the surface roughness decreases indirectly enhancing the antifouling property of membranes. The adsorption capacity of bovine serum albumin on the membrane surface decreased from 2.85 to 2.15 mg cm^{-2} as the TiO_2 loading increased from 0 to 0.02 g TiO_2/g PVDF. Fouling was found due to cake formation in ultrafiltration and can be explained by Hermia's fouling model suggesting that the solutes are not deposited into the pores, which indicates that the fouling process is physically reversible.

Keywords: Membrane, Hydrophilicity, Permeation, Ultrafiltration, Fouling

INTRODUCTION

Due to its non-toxic nature, reasonably high chemical resistance and relatively low cost, polyvinylidene fluoride (PVDF) is one of the widely used polymers for making membranes for ultrafiltration (UF). However, high hydrophobicity restricts its application and fouling reduces its performance. Fouling of MF and UF membranes due to proteins has been ascribed to adsorption and deposition of proteins on the membrane surface and within their pores [1].

Membrane fouling of UF membranes strongly affects the economic and technological viability of the process [2]. Some types of membrane fouling (reversible fouling) can be eliminated by the physical cleaning because the solutes are externally deposited on the membrane, whereas other types (irreversible fouling) requires chemical cleaning [3] because they get accumulated inside the pores and the attachment strength of particles is higher in this case compared to reversible. The chemical cleaning after permeation affects the membrane material, thus adversely affecting membrane life. This has necessitated the modification of membranes to improve the performance without fouling.

Various modification techniques used for this purpose include physical blending with hydrophilic fillers (polymers or inorganic), grafting of hydrophilic species, and plasma treatment to improve the hydrophilicity of PVDF membranes [4-7], but these techniques suffer from weak interaction during physical blending between the polymer and additives, reducing the long-term durability and instability due to an additive release from the membranes [5]. Recently, nanocomposite membranes, i.e., polymer embedded with uniformly dispersed inorganic nanoparticles (NPs), have attracted attention due to unique physicochemical properties of NPs [8,9]. Incorporation of NPs in the polymer matrix alters the porous structure and improves hydrophilicity and mechanical, thermal, permeability and antifouling properties [5]. Nano-particles of TiO_2 [10], ZnO [11], SiO_2 [12], GO [5] are widely used for the synthesis of polymer-inorganic membranes [13].

Fouling is normally classified as reversible fouling which can be eliminated by physical cleaning and irreversible fouling requiring certain pretreatment [14]. A better understanding of fouling in the membrane is important to solve the problems for its successful application. A thorough study of membrane fouling will be advantageous to determine the capacity and efficiency of the membrane at certain conditions. Several empirical and mathematical models have been developed to explain the membrane fouling mechanism [15-17] and to define the flux decline with time. Mathematical models are useful for optimization of fouling removal and prevention methods along with better process understanding of filtration phenomena in the different membrane in real-world scenarios, Completely theoretical models have failed to explain the permeate flux decline during ultrafiltration without using experimental data [17,18]. Therefore, semi-empirical models that permit accurate prediction of the flux decline during ultrafiltration and offer explanation to the process of fouling are preferred. Hermia's model is one such model that was used in this work to quantify the properties of the membrane by fitting the experimental result to explain the fouling mechanism

†To whom correspondence should be addressed.
E-mail: zeenata.rs.che15@itbhu.ac.in

in order to adapt the process in controlling the fouling. The parameter of this model has a physical meaning and is based on classical constant pressure filtration equations, and compared to another model it does not involve complex mathematical equations.

In the present work, green synthesized TiO_2 NPs embedded PVDF membranes with different weight fractions of TiO_2 NPs were prepared via the phase inversion method. The antifouling performance of synthesized membrane was investigated using BSA, the model foulant and Hermia model to investigate the fouling phenomenon and associated mechanism during UF process and also to quantify the membrane properties on fouling. The model predictions data was compared with the experimental data to study the effect of TiO_2 NPs on the fouling (reversible and irreversible) occurring compare to pure PVDF.

EXPERIMENTAL

1. Materials

Polyvinylidene fluoride (PVDF), n-methyl-2-pyrrolidone (NMP), Titanium isopropoxide (TTIP) were obtained from Sigma-Aldrich. Bovine serum albumin (BSA) was obtained from SDFine Chemicals Ltd. (Bombay), and phosphate buffer saline (PBS) was obtained from Merck, (India). Double distilled water (DD) used in all experiments was prepared in the laboratory.

2. Synthesis of TiO_2 Nanoparticles (NPs)

Arhar pulse (Dal) (split and dehusked *Cajanus cajan* seeds) collected from the local grain market were thoroughly washed with clean water first and then thrice with distilled water to remove surface dust. About 10 g of the washed pulse particles were soaked in 50 mL distilled water taken in a Borosil glass beaker and heated (80 °C) for 3 h. The extract thus obtained was filtered through a Whatman No-01 filter paper, and the filtrate was collected and used for the synthesis of TiO_2 nanoparticles.

90 ml of 5 mM TTIP solution (precursor) was added to 30 ml of pulse extract (reducing agent) in the ratio of 9 : 3 (v/v) and the mixture was stirred continuously at the ambient temperature for 7 h. The mixture was centrifuged (High-Speed Research Centrifuge-TC 4100 F) at 9,000 rpm for 20 min to separate the powder from the extract. The obtained TiO_2 NPs were dried at 100 °C for overnight followed by calcination at 570 °C in a muffle furnace for 2.5 h. The TiO_2 NPs thus prepared were then immobilized in a PVDF polymer matrix in known amounts to obtain polymeric composite membranes.

3. PVDF/TiO_2 Composite Membrane Preparation

The PVDF composite membranes were fabricated using the phase-inversion method via the immersion precipitation technique. Prior to the experiment, to remove moisture, the PVDF pellets were dried in an air oven at 80 °C for 24 h. A homogeneous polymeric solution was prepared by dissolving 2 g of the dried PVDF pellets in 10 ml of NMP, an organic solvent using a magnetic stirrer maintained at a temperature of around 70 °C for 3 h. In the meantime, different amounts of synthesized TiO_2 (0.02, 0.04 and 0.06 g) were added to 4 ml of NMP and stirred at room temperature for 1 h followed by sonication for 2 h at 50 kHz to ensure homogeneous dispersion of particles. These suspended TiO_2 NPs were added to the previously prepared 10 ml of PVDF-NMP dope solution and were continuously stirred for 8 h at 70 °C at 500 rpm to achieve a uniform suspension. The solution was then cast as a film on a glass plate to produce flat sheet membrane (with a thickness of 180 μm) and exposed to air for 30 s for partial solvent evaporation. These glass plates were then placed in a water bath to remove all residual solvent at ambient temperature (27±1 °C) for 24 h to form membrane via the phase inversion method. The fabricated membranes were peeled off, washed and stored under water to make them ready for characterization. PVDF membranes of varying TiO_2 loading are named as P1 (0 g TiO_2/g PVDF), P2 (0.01 g TiO_2/g PVDF), P3 (0.02 g TiO_2/g PVDF) and P4 (0.03 g TiO_2/g PVDF).

4. Membrane Characterization

The synthesized TiO_2 NPs were characterized by the Smart Lab X-Ray diffractometer (Rigaku) to analyze their crystal structure and phase. The equipment operates at 18 kW using a rotating anode (1,200-1,800 K temperature) equipped with Cu-Kα radiation (λ= 0.154 nm) within a 2θ range of 10°-80° at 40 kV/15 mA.

The average particle size and the particle size distribution were calculated using Nano Plus (zeta/nanosize analyzer) based on the principle of dynamic light scattering technique.

Scanning probe microscope (NTEGRA Prima) was employed to analyze the surface roughness of the membrane noncontact mode. Membrane pieces of approximately 1 cm^2 were dried at ambient temperature prior to the measurements, and all the measurements were carried at atmospheric pressure. These pieces were secured on a microscope glass slide with the help of double-sided tape to avoid wrinkles. The surface of the membrane was scanned within the scanning area of 5 μm×5 μm. The data obtained were analyzed using Nova Px 3.2.5 software.

A static contact angle between the membrane surface and water droplet was measured with a goniometer [KRUSS, Germany] to investigate the membrane hydrophilicity using a sessile drop. The average of five measurements at random locations for each membrane sample was reported to reduce experimental error.

5. BSA Adsorption Experiment

Pure PVDF and nanocomposite membranes of size 1×1 cm^2 were taken and immersed into 5 mL of BSA (0.5 g/L in 5 mM PBS, pH=7.5) to carry out adsorption at room temperature for 24 h till equilibrium was attained. Then, the samples with adsorbed BSA were removed, and the remaining solution in the vials was agitated in a shaker. The BSA concentration was measured using a UV spectrophotometer (SYSTRONICS, PC based Double Beam Spectrometer 2202). To minimize error, each reported value was obtained by averaging five individual measurements. The BSA adsorption capacity was determined using Eq. (1) [19]

$$\text{Adsorption capacity} = \frac{C_0 - C}{A} \times V \quad (1)$$

where A is the area of membrane (m^2), V is total volume (5 mL), and C_0 and C are the concentration of BSA before and after contact with the membranes.

6. Fouling Quantification

The effect of TiO_2 loading on membrane performance and fouling behavior was investigated using BSA as the model foulant. The BSA solution was prepared by dissolving 1 g BSA in 1 L of 1 mM of PBS solution at pH 7.5. The filtration experiments were carried

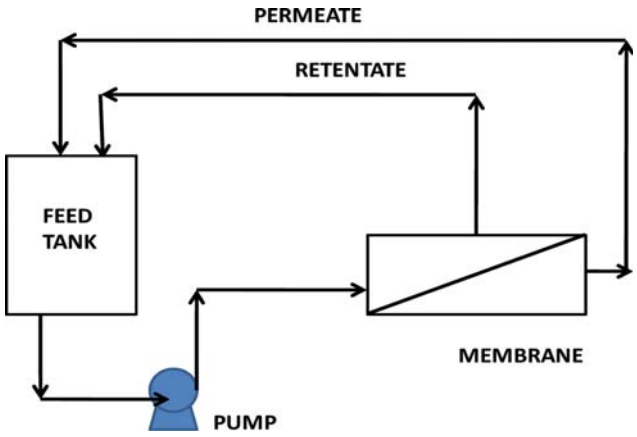

Fig. 1. The dead-end filtration cell.

out in a dead-end filtration setup as shown in Fig. 1.

The effective membrane area for filtration was 15.5 cm^2. The membranes were initially pre-pressurized for 30 min at 2 bar to achieve stable water flux. After pure water flux measurement (J_{w1}) tests, the flux for BSA solution was measured (J_{BSA}) and was recorded every 10 min to determine the dynamic fouling resistance. After 2 h of BSA filtration, the fouled membrane was rinsed with distilled water for 30 min under magnetic stirring for 30 min, and then second pure water flux (J_{w2}) was again measured. All the measurements were at 2 bar at 27±°C. To measure the ability for the recovery of the fouled membrane concentration of BSA in feed (C_f) and permeate (C_p) was determined using UV spectrophotometer and was calculated using Eq. (2).

$$\text{Flux recovery ratio (FRR)} = \frac{J_{w2}}{J_{w1}} \times 100 \tag{2}$$

6-1. Fouling Resistance

The loss in flux is due to three parameters: i) reversible fouling rate (RFR), ii) irreversible fouling rate (IFR), and iii) total fouling ratio (TFR) of the membrane; each of these was calculated using following equations [20,21]

$$\text{RFR \%} = \left(\frac{J_{w2} - J_{BSA}}{J_{w1}}\right) \times 100 \tag{3}$$

$$\text{IFR \%} = \left(\frac{J_{w1} - J_{w2}}{J_{w1}}\right) \times 100 \tag{4}$$

and

$$\text{TFR \%} = \text{RFR \%} + \text{IFR \%} = \left(\frac{J_{w1} - J_{BSA}}{J_{w1}}\right) \times 100 \tag{5}$$

7. Fouling Mechanism: Hermia's Model

Hermia's model, the most comprehensive fouling prediction model, is used to identify the dominant mechanism responsible for membrane fouling under constant pressure filtration. The understanding of the fouling mechanism will provide a path to adapt process in controlling the membrane fouling. The model provides a correlation between flux and operating time by assuming pore blockage, gel-polarization, and bio-fouling. In general mathematical form it is expressed as [18]:

$$\frac{d^2t}{dV^2} = \alpha\left(\frac{dt}{dV}\right)^n \tag{6}$$

where V is the cumulative volume of filtrate (m^3), α is the proportionality constant, t is the time of filtration, A is flow area (m^2), and n is the constant characterizing the fouling model. The flux (J) of the permeate is written as

$$J = \frac{1}{A}\frac{dV}{dt} \tag{7}$$

Eq. (7) can be rewritten as

$$dt/dV = 1/AJ$$

The second derivative of Eq. (7) gives

$$\frac{d^2t}{dV^2} = -\alpha A^{-2} J^{-3}\frac{dJ}{dt} \tag{8}$$

Eq. (8) is proportional to the rate of increase in total resistance [19]. The rate governing equation for flux decline with time now becomes

$$\frac{dJ}{dt} = -\alpha A^{2-n} J^{3-n} = -K_{CF} J^{3-n} \tag{9}$$

where K_{CF} is a phenomenological coefficient that permits a deeper analysis of the fouling mechanisms taking place inside pores or onto the membrane surface. The model represented in Equation 9 is used to distinguish four possible fouling mechanisms and their phenomenological coefficients.

7-1. Complete Pore Blockage (n=2)

The linear form for this model was derived by integrating Eq. (9) with time and substituting n=2.

$$\ln\left(\frac{1}{J}\right) = \ln\left(\frac{1}{J_o}\right) + K_1 t \tag{10}$$

where K_1 represents complete pore blocking coefficient; it is determined by evaluating the slope from the straight line fitting of Eq. (10).

According to this model, the flux decline is due to the deposition of the solute aggregates of a larger size than the membrane pore size on the membrane surface, thereby decreasing the available pores for the filtrate to pass through it or, in other terms, the entrance of the pores is sealed.

7-2. Standard Pore Blocking (n=1.5)

This approach accounts for the fouling occurring within the internal structure of the membrane. The reduction of pore radii is due to deposition or adsorption of the solute onto the internal pore walls. Taking the value of exponent n in Eq. (9) as 1.5 and integrating it to give the linear form of flux decline relation with time as:

$$\left(\frac{1}{\sqrt{J}}\right) = \left(\frac{1}{\sqrt{J_o}}\right) + K_2 t \tag{11}$$

where K_2 represents internal pore blocking coefficient; it is determined by evaluating the slope from the straight line fitting of Eq. (11).

7-3. Intermediate Pore Blockage (n=1)

This model is similar to the complete pore blockage model. Also,

it describes blockage or obstruction of the entrance of the pore without completely blocking it. Particles here get deposited on the pores wall, thus reducing the pore volume. The irregularity of passage through pore causes the particle tightly fixed with the pore. Substituting n=1 in Eq. (9) and integrating with time, define the linear form of flux decline of this model:

$$\left(\frac{1}{J}\right)=\left(\frac{1}{J_o}\right)+K_3t \quad (12)$$

where K_3 represents intermediate pore blocking coefficient; it is determined by evaluating the slope from the straight line fitting of Eq. (12).

7-4. Cake Filtration (n=0)

In contrast to the above-described models, here it is assumed that the fouling occurs by the formation of cake over the membrane surface, thereby increasing the hydraulic resistance. The overall resistance is a combination of cake resistance and resistance of membrane. The filtration model is obtained by substituting n=0 and integrating Eq. (9):

$$\left(\frac{1}{J^2}\right)=\left(\frac{1}{J_o^2}\right)+K_4t \quad (13)$$

where K_4 represents cake pore block coefficient. It is determined by evaluating the slope from the straight line fitting of Eq. (13).

whereas in Eqs. (10)-(13) J_o is initial permeate flux, J is flux at time t.

RESULTS AND DISCUSSION

1. Particle Structure and Size

The XRD patterns of the synthesized TiO_2 NPs are shown in Fig. 2(a). The strong and sharp peaks indicate the excellent crystalline structure of nanoparticles. The diffraction peaks at 2θ of 25.3°, 37.8°, 48.01°, 54.6°, and 68.76° correspond to the anatase phase of TiO_2 NPs with Miller indices (hkl) values of (101), (004), (200), (211), (116) (JCPDS 21-1272) [23].

This confirms the particle synthesized using Dal extract is TiO_2 NPs. The crystalline size of the particle was also calculated using Debye Scherrer's equation:

$$d=0.89\,\lambda/\beta\cos\theta \quad (14)$$

Table 1. Roughness parameter of PVDF and its composite membrane

Sample	R_a (nm)	R_q (nm)	R_z (nm)
P1	25.64	23.76	74.54
P2	20.16	22.68	62.48
P3	07.48	08.12	25.92
P4	14.14	15.03	40.88

where d is the crystalline size of NPs (nm), λ is the wavelength of X-ray (0.154 nm), θ is Bragg's diffraction angle, and β is the full width at half maximum (FWHM). The crystalline size of the synthesized NPs was found to be 10.5 nm. These results suggest that the synthesized TiO_2 particles are of nanosize and are of anatase phase.

The average particle size was calculated using the data obtained through dynamic light scattering (DLS) technique, and a broad particle size distribution was observed in the range 10 to 25 nm (Fig. 2(b)).

2. Surface Morphology of Membranes

Fig. 3 shows the 2D AFM images (5.0 μm×5.0 μm) of different type PVDF/TiO_2 composite membranes and roughness parameters were obtained using AFM analysis software Nova Px 3.2.5. The data in Table 1 lists the three different roughness parameters: i) mean roughness (R_a) represents the deviation of the z-values and is taken as half the average peak to valley depth, ii) root mean square roughness (R_q) takes into consideration the standard deviation of z-values in certain area, and iii) average of height (R_z) is defined as the difference of largest positive and negative z-values [24].

From Fig. 3 it is seen that with an increase in the loading of TiO_2, surface roughness decreases and is maximum for P1 (0 g TiO_2/g PVDF), which implies that the modified composite membrane had a smoother surface and a denser skin [24,25]. This decrease in roughness parameter implies excellent antifouling ability of the polymeric membrane. The decrease in roughness will minimize the penetration and adhesion of contaminants into the valleys and peaks, respectively. This decline can also be explained by filling of the membrane pores by the entrapped TiO_2 nanoparticles in the polymeric matrix. However, it was also observed that excessive addition of TiO_2 particles in the matrix as in the case of P4 (0.03 g TiO_2/g PVDF) results in agglomeration of the particle at high con-

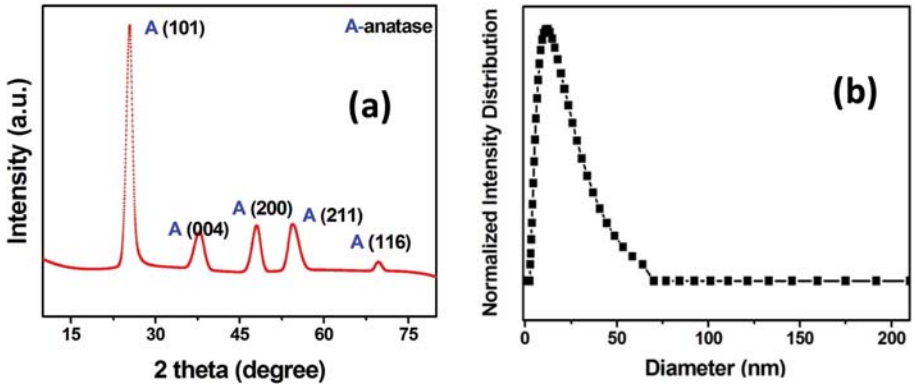

Fig. 2. (a) XRD pattern of TiO_2 NPs and (b) Particles size data of TiO_2 NPs.

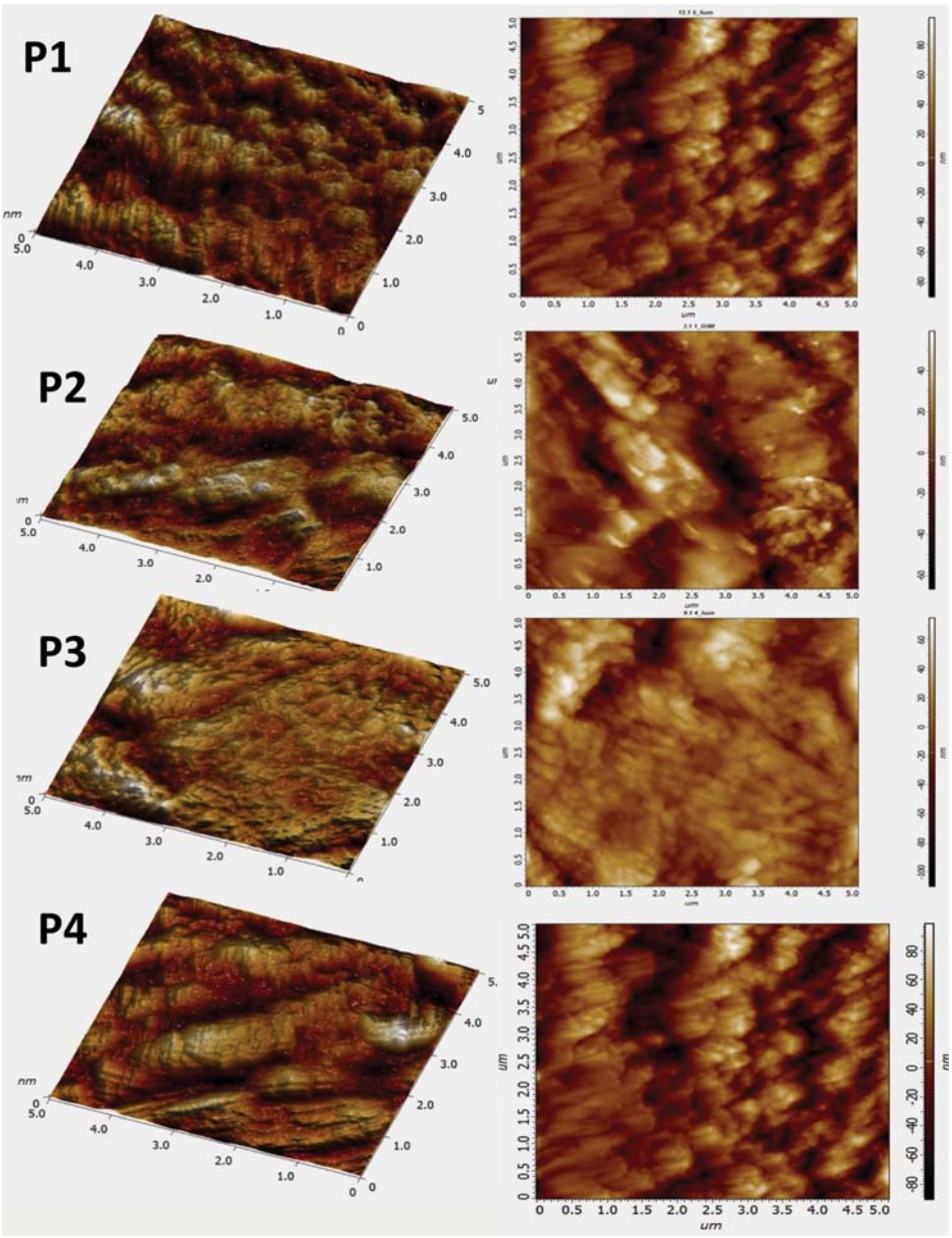

Fig. 3. 2D AFM images of different composite membranes.

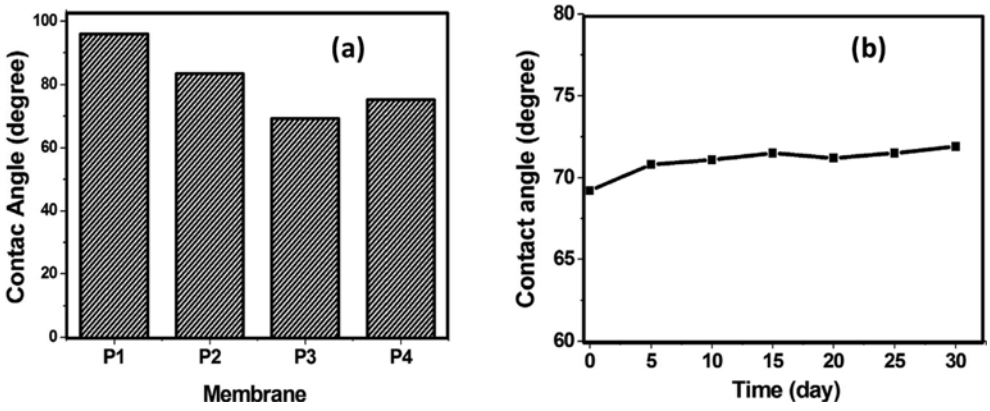

Fig. 4. (a) Water contact angle of the different composite membrane and (b) Water contact angle changes of P3 membrane for a different period.

centration, which results in the bump formation due to which peak value increases and roughness increases [26]. The observed surface roughness value of the tested membrane was compared and justified with permeate flux decline. It was also demonstrated that the membrane with the lowest surface roughness value has the lowest permeate flux decline.

3. Surface Hydrophilicity and Wetting Ability of Pure and Composite Membranes

Contact angles of membranes surface provide information regarding surface hydrophilicity of the membrane. The contact angle value of different membrane is shown in Fig. 4(a). The surface hydrophilicity is one of the important parameters affecting the filtration through the membrane. From Fig. 4(a), the contact angle declines gradually from 85.9° to 69.2°, suggesting the increase in hydrophilicity. Mainly, there are three parameters responsible for the decay rate of contact angle: i) hydrophilicity of the membrane surface, ii) pore size, and iii) wettability [27]; and in this study, it is due to the increasing concentration of hydrophilic TiO_2 NPs having high affinity towards water. It was also observed that at maximum loading TiO_2 (0.03 g TiO_2/g PVDF, P4), this value increases to 75.2°; the high concentration leads to the particle aggregation, which results in the non-uniform distribution of particles causing an increase in contact angle values.

It is possible that some TiO_2 may come out of the polymer matrix during the filtration process and can affect the hydrophilicity of membrane; hence, the stability of the particle on membrane surface is also important and was investigated by measuring the variation in contact angle value which acts as a stability indicator of membrane hydrophilicity. The membrane P3 (chosen as the sample membrane) was immersed in water at ambient temperature and shaken continuously. Fig. 4(b) shows the change in contact value with time. It is observed that for P3 membrane before shaking the initial contact angle value 69.2° (zero-day), slightly increased to 71.5° during the 15th day. However, no further change was observed, and value retains at 71.8° even after a 30th day. This indicates excellent stability of NPs within the membrane matrix.

4. BSA Adsorption Test

As mentioned, the TiO_2 incorporated PVDF membranes exhibit enhanced hydrophilicity due to the presence of hydrophilic TiO_2 within the polymer matrix. Enhanced hydrophilicity directly improves the anti-fouling properties of membranes. The static protein adsorption was investigated to study the anti-fouling properties. As shown in Fig. 5, the saturated mass of the static BSA adsorption decreases with increase in TiO_2 loading from 0 to 0.02 g TiO_2/g PVDF. Decreased adsorption values suggest increased anti-fouling ability. It is attributed to the fact that the presence of abundant surface hydroxyl on the entrapped TiO_2 nanoparticles weakens the hydrophobic interaction of membranes with BSA, and thus decreases the adsorption and attachment of foulants. However, due to agglomeration of particles at 0.03 g TiO_2/g PVDF, the adsorption value increases because of uneven distribution of particles creating space for the protein adsorption to take place, hence significantly less protein resistant compared to P3 (0.02 g TiO_2/g PVDF).

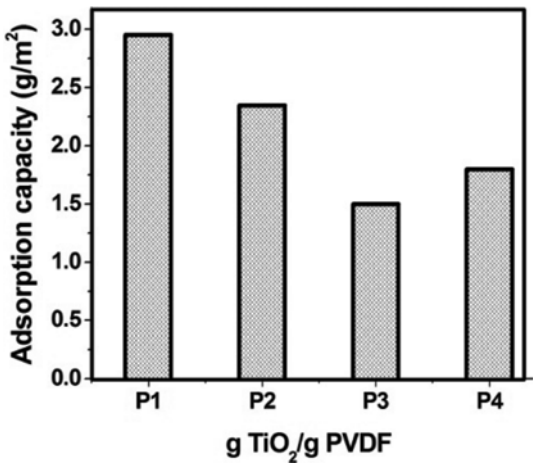

Fig. 5. Adsorption capacity at different TiO_2 loading.

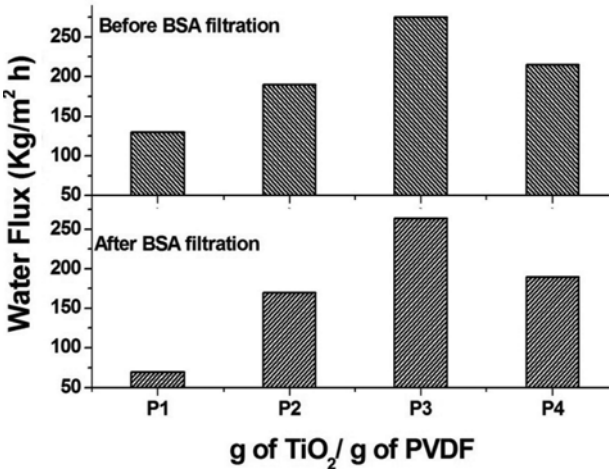

Fig. 6. Pure water flux before and after filtration.

5. Water Permeation through Membranes

Fig. 6 shows the effect of TiO_2 loading in the membrane on the pure water flux before and after BSA filtration. It is seen that the increase in the water flux for TiO_2 incorporated membranes follows the same trend of hydrophilicity increase. It can be concluded that the increased membrane's hydrophilicity increases the water permeability by attracting water molecules and facilitating the permeation through the membrane. Moreover, the enhancement in the flux is due to an increase in porosity and pore size. During the phase inversion process, an increase in the diffusion of solvent from the membrane to water facilitates the formation of a large number of micro-pores, leading to the formation of a porous membrane [28]. The TiO_2 incorporated membrane with the highest loading (P4) gives less water flux than P2 and P3 membranes. This is attributed to the tendency of inorganic nanoparticles to aggregate at high concentrations [29] and plug the membrane pores, resulting in a decline in the pure water flux. In this study, the maximum pure water flux was achieved for membrane P3 with optimum TiO_2 loading of 0.02 g/g PDVF. This can be attributed to the proper dispersion of inorganic nanoparticles at the optimum loading. The AFM photo-micrographs shown in Fig. 3 also support this observation.

To further investigate the antifouling property of TiO_2 incorporated PVDF membranes, the flux recovery ratio (FRR (%)) and foul-

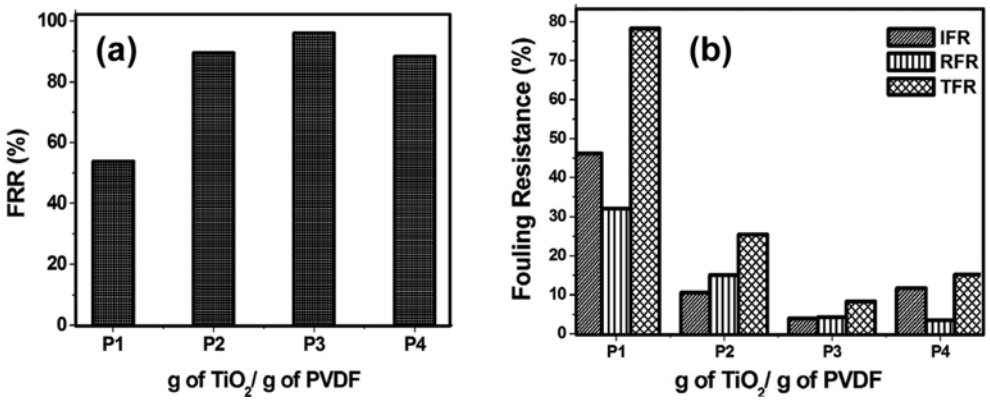

Fig. 7. (a) FRR in membranes and (b) Fouling resistance in membranes.

ing resistance were also evaluated and results are shown in Fig. 7(a) & (b). A high value of FRR represents an excellent antifouling property of the membrane. Only 53.84% FRR was achieved using bare PVDF, which was very small compared to hybrid membranes. The FRR value (%) of all PVDF/TiO_2 membranes was more than 85%, and the maximum 96% was obtained for the P3 membrane. The obtained results of FRR are in good agreement with the results of AFM in Table 1. The table result shows that the surface roughness parameter for the pure PVDF membranes is significantly higher than the hybrid membranes. The increase in rough surface increases the fouling ability of membrane due to protein accumulation within the "valleys". In this study, the membrane P3 (0.02 g TiO_2/g PVDF) showed the lowest roughness parameters, which means the smoothest surface and low contact angle value with high hydrophilicity results in the best flux recovery ratio due to less deposition of foulant on the smoother surface (Fig. 7(a)).

To study the details of fouling process in membranes, total fouling ratio (TFR), reversible fouling ratio (RFR) and irreversible fouling ratio (IFR) were evaluated for all of the prepared membranes using Eqs. (3) to (5). The reversible fouling refers to the weak binding of foulant species to the membrane surface and can be eliminated easily by water washing. This is an important parameter as fouling of membrane increases the operational costs [29]. The irreversible fouling, the foulants are strongly attached to the mem-

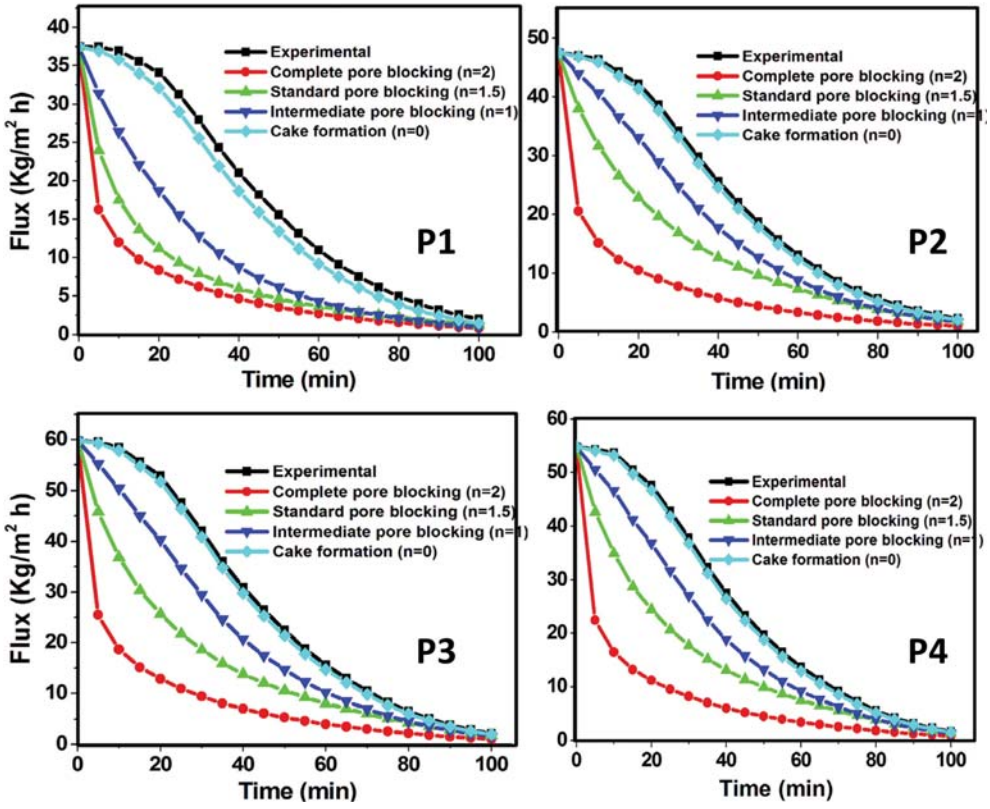

Fig. 8. Experimental filtration data and classic fouling models for membrane.

Table 2. Values of k and R^2 in Hermia's fouling model for composite membranes

Sample	Cake pore		Intermediate pore		Standard pore		Complete	
	n=0		n=1		n=1.5		n=2	
	R^2	K_4	R^2	K_3	R^2	K_2	R^2	K_1
P1	0.897	0.030	0.77	0.150	0.621	0.210	0.394	0.230
P2	0.944	0.003	0.88	0.129	0.811	0.110	0.648	0.180
P3	0.959	0.002	0.91	0.099	0.840	0.101	0.683	0.150
P4	0.957	0.001	0.92	0.011	0.860	0.014	0.683	0.018

brane surface and are removed by the chemical cleaning process. So, this type of fouling deteriorates the membrane lifetime along with increases the process complexity [30]. The calculated TFR, RFR, and IFR are shown in Fig. 7(b). The figure shows that the pure membrane has the highest TFR (78.28%) and IFR (46.15%) while values are reduced significantly in case of composite membranes this is attributed to the surface hydrophilization due to the incorporation of TiO_2 NPs thereby changing the hydrophobic property and pore surface of pure PVDF membrane. Presence of NPs reduces the adsorption ability (Fig. 5) because the interaction between foulant and hydrophobic membrane interfaces (P2, P3, and P4) diminishes, thus weakened anchoring effect promotes easy cleaning of BSA foulant by water flushing during filtration. The protective hydration layer over the membrane surface because of adsorption of water molecule due to the presence of hydrophilic TiO_2 NPs will exclude the BSA molecule more effectively [30]. It was also observed that with increasing TiO_2 loading (P2 and P3) membrane the resistance value decreases and minimum for P3 membrane and has a promising performance compared to bare PVDF.

6. Hermia Model

Hermia's model was used to study the flux decline, and various parameters determined using the model are shown in Fig. 8 and Table 2, respectively. The type of pore blocking and a fitting degree of a model for fouling was selected based on the highest value of R linear regression obtained using Eqs. (10) to (13) from section 7.

If the size of foulant is smaller than the membrane pores, standard pore blocking occurs. However, when the foulant gets adsorbed on the membrane pore walls, it reduces the pore volume. From Fig. 8 it is observed that the standard pore blocking model deviates to a larger extent for all membranes compared to the experimental data, so it is not a well-accepted model to determine fouling in the membrane. This is because most of the foulant is retained by the membrane at the operating conditions since most of the foulant present in feed solution is larger than the membrane pores [2]. Similar is the case for the complete pore blocking model. High deviation was observed between experimental and predicted flux because the larger size of the molecule leads to poor fitting of the model.

In case of intermediate pore blockage, when the size of membrane pores is similar to the foulant molecule size, the entrance of the pores on the feed side is blocked. The predicted flux, in this case, provides a better agreement with the experimental data compared to the standard and complete pore blockage models. Further, it has been reported that the UF is accurately described by the intermediate pore blocking model [2,31]. The pore blockage due to cake formation occurs when the solute size is larger than the membrane pore size; as a result, the solute molecules are not able to enter the membrane pores and accumulate over the surface forming a layer. The deposition of the solute layer over the membrane surface exerts additional resistance to the fluid flow through the membrane [32,33]. Model prediction is observed to be in very good agreement with the experimental flux data (Fig. 8) at the tested experimental conditions. The high R^2 value indicates a better fit for this model. Further, the values predicted by the intermediate pore blockage model for all four membranes are closer to the experimental flux.

It can be suggested that the primary fouling mechanisms are the cake formation and intermediate pore blockage. Thus, it is possible to infer that most of the area of the fouled membrane gets covered due to cake formation, while over some area the particles enter the pores and lead to pore-constrictions. Table 2 result shows that for the various membranes, pore block coefficients in all cases decline with increasing concentration of TiO_2 and are having the least value in cake filtration (n=0). This implies that as the rate of deposition of foulant over the membrane reduces, the concentration polarization gets alleviated leading to a reduction in the cake layer fouling [33].

Therefore, using the Hermia fouling model for analysis of flux data it can be inferred that it is not the pore blockage; rather, it is the cake layer that is responsible for fouling in all four different membranes. It means that the solute is not adsorbed on the inner side of the pores. Thus it can be inferred that the fouling process is physically reversible [32].

CONCLUSION

Low-cost TiO_2 nanoparticles of size 10.5 nm were successfully synthesized by green route. Low fouling membranes using PVDF as a polymer base and TiO_2 nanoparticles as an additive (synthesized by a green route) were prepared using the phase inversion technique. The good TiO_2 dispersion on PVDF membrane plays a significant role in the membrane antifouling property. The ultrafiltration performance and anti-fouling property of the membrane were investigated using BSA as the model foulant. The low value of TFR and IFR for nanocomposite membrane results suggested that addition of very small quantity of TiO_2 nanoparticles (0.02 g TiO_2/g PVDF) enhanced the resistive fouling property of membrane by decreasing the irreversible fouling followed by an increase in the portion of reversible fouling. This will result in easy removal of fouling by physical cleaning. The fouling mechanism was also analyzed

using four modes of Hermia's fouling model and we observed that the "cake filtration" model gave the best representation of pore blocking, which further justifies that the fouling process is physically reversible. The increase in surface hydrophilicity of the nanocomposite membrane showed more reversible fouling compared to neat PVDF membrane.

ACKNOWLEDGEMENT

The authors acknowledge Central Instrument Facility, IIT (BHU) for AFM characterization facility.

REFERENCES

1. A. D. Marshall, P. A. Munro and G. Tragardh, *Desalination*, **91**(1), 65 (1993).
2. A. Salahi, M. Abbasi and T. Mohammadi, *Desalination*, **251**, 153 (2010).
3. H. Etemadi, R. Yegani, M. Seyfollahi and M. Rabiee, *Iran. Polym. J.*, **27**, 381 (2018).
4. E. Shokri, R. Yegani, S. Heidari and Z. Shoeyb, *Chem. Eng. Res. Des.*, **100**, 237 (2015).
5. C. Zhao, X. Xu, J. Chen and F. Yang, *Desalination*, **334**, 17 (2014).
6. C. Zhao, X. Xu, J. Chen, G. Wang and F. Yang, *Desalination*, **340**, 59 (2014).
7. A. Behboudi, Y. Jafarzadeh and R. Yegani, *Chem. Eng. Res. Des.*, **114**, 96 (2016).
8. A. Akbari, R. Yegani, B. Pourabbas and A. Behboudi, *Chem. Eng. Res. Des.*, **109**, 282 (2016).
9. H. Etemadi, R. Yegani and V. Babaeipour, *Diam. Relat. Mater.*, **69**, 166 (2016).
10. Y. Jafarzadeh and R. Yegani, *Chem. Eng. Res. Des.*, **93**, 684 (2015).
11. S. Balta, A. Sotto, P. Luis, L. Benea, B. Van der Bruggen and J. Kim, *J. Membr. Sci.*, **389**, 155 (2012).
12. X. Zuo, L. Wang, J. He, Z. Li and S. Yu, *Desalination*, **347**, 43 (2014).
13. S. Zinadini, V. Vatanpour, A. A. Zinatizadeh, M. Rahimi, Z. Rahimi and M. Kian, *J. Water Process Eng.*, **7**, 280 (2015).
14. P. K. Bhattacharya, S. Agarwal, S. De and U. V. S. Rama Gopal, *Sep. Purif. Technol.*, **21**, 247 (2001).
15. C. Bhattacharjee and S. Datta, *Sep. Purif. Technol.*, **33**, 115 (2003).
16. A. L. Zydney and C.-C. Ho, *Desalination*, **146**, 75 (2002).
17. M. C. V. Vela, S. A. Blanco, J. L. García and E. B. Rodríguez, *Sep. Purif. Technol.*, **62**, 489 (2008).
18. A. Charfi, N. B. Amar and J. Harmand, *Water Res.*, **46**, 2637 (2012).
19. Y. H. Teow, B. S. Ooi and A. L. Ahmad, *J. Water Process Eng.*, **15**, 89 (2017).
20. Li-L. Hwang, Hui-H. Tseng and J-C Chen, *J. Membr. Sci.*, **384**, 72 (2011).
21. H. Etemadi, R. Yegani and M. Seyfollahi, *Iran. Polym. J.*, **27**, 381 (2018).
22. M. Safarpour, A. Khataee and V. Vatanpour, *Sep. Purif. Technol.*, **140**, 32 (2015).
23. Q. Wang, Z. Wang, J. Zhang, J. Wang and Z. Wu, *RSC Adv.*, **4,** 43590 (2014).
24. N. Meng, R. C. E. Priestley, Y. Zhang, H. Wang and X. Zhang, *J. Membr. Sci.*, **501**, 169 (2016).
25. C. Zhao, X. Xu, J. Chen and F. J. Yang, *Environ. Chem. Eng.*, **1**, 349 (2013).
26. J.-H. Li, Y.-Y. Xu, L.-P. Zhu, J.-H. Wang and C.-H. Du, *J. Membr. Sci.*, **326**, 659 (2009).
27. J. H. Jung, H. Kobayashi, K. J. C. van Bommel, S. Shinkai and T. Shimizu, *Chem. Mater.*, **14**, 1445 (2002).
28. S. Zinadini, A. A. Zinatizadeh, M. Rahimi, V. Vatanpour and H. Zangeneh, *J. Membr. Sci.*, **453**, 292 (2014).
29. J.-Y. Tian, M. Ernst, F. Cui and M. Jekel, *Water Res.*, **47**, 1218 (2013).
30. S. Peldszus, C. Hallé, R. H. Peiris, M. Hamouda, X. Jin, R. L. Legge, H. Budman, C. Moresoli and P. M. Huck, *Water Res.*, **45**, 5161 (2011).
31. J. Lee, S. Jeong, Y. Ye, V. Chen, S. Vigneswaran, T. Leiknes and Z. Liu, *Sep. Purif. Technol.*, **176**, 323 (2017).
32. M. Fonouni, H. Etemadi, R. Yegani and S. Zarin, *Desalination Water Treat.*, **90**, 99 (2017).
33. Y. Zheng, W. Zhang, B. Tang, J. Ding, Y. Zheng and Z. Zhang, *Bioresour. Technol.*, **250**, 398 (2018).